Article

Metastability of diamond ramp-compressed to 2 TPa

https://doi.org/10.1038/s41586-020-03140-4

Received: 1 June 2020

Accepted: 26 October 2020

[redacted]

Check for updates

A. Lazicki[1]✉, D. McGonegle[2], J. R. Rygg[3,4,5], D. G. Braun[1], D. C. Swift[1], M. G. Gorman[1], R. F. Smith[1], P. G. Heighway[2], A. Higginbotham[6], M. J. Suggit[2], D. E. Fratanduono[1], F. Coppari[1], C. E. Wehrenberg[1], R. G. Kraus[1], D. Erskine[1], J. V. Bernier[1], J. M. McNaney[1], R. E. Rudd[1], G. W. Collins[3,4,5], J. H. Eggert[1] & J. S. Wark[2]

Carbon is the fourth-most prevalent element in the Universe and essential for all known life. In the elemental form it is found in multiple allotropes including graphite, diamond and fullerenes, and it has long been predicted that even more structures can exist at pressures greater than those of Earth's core[1–3]. Several phases have been predicted to exist in the multi-terapascal regime, which is important for accurate modelling of the interiors of carbon-rich exoplanets[4,5]. By compressing solid carbon to 2 terapascals (20 million atmospheres; more than five times the pressure at Earth's core) using ramp-shaped laser pulses, and simultaneously measuring nanosecond-duration time-resolved X-ray diffraction, we found that solid carbon retains the diamond structure far beyond its regime of predicted stability. The results confirm predictions that the strength of the tetrahedral molecular orbital bonds in diamond persists under enormous pressure, resulting in large energy barriers that hinder conversion to more-stable high-pressure allotropes[1,2], just as graphite formation from metastable diamond is kinetically hindered at atmospheric pressure. This work nearly doubles the highest pressure at which X-ray diffraction has been recorded on any material.

On Earth, carbon can exist in a number of different allotropes, with graphite and diamond being the most well known, although several others exist[6–8], or have been predicted to be stable[9–11]. Diamond, the face-centred-cubic form of carbon (with space group $Fd\bar{3}m$, here called FC8) has many technologically important properties owing to its compressive strength and high thermal conductivity. The phase diagram of carbon at pressures in the terapascal (TPa) regime is directly relevant to the structure of planets within our Solar System and beyond[4,5]. Theoretical calculations based on density functional theory (DFT) of the crystalline phases of carbon at TPa-scale pressures have a long history[1–3,12–14], with general agreement emerging that body-centred-cubic (BC8; $Ia\bar{3}$) and simple-cubic (SC1; $Pm\bar{3}m$, and SC4; $P4_332$) phases are lower in enthalpy than FC8 above about 1 TPa, with BC8 being the first to satisfy this condition at around 1 TPa (Fig. 1).

Multi-TPa pressures far exceed those that can be achieved under static conditions in the laboratory using anvils[15,16]. Although such high pressures can be obtained with shock compression, this highly entropic process starts to melt diamond above 0.6 TPa, according to a study of changes in entropy manifested in decaying shock waves[17] (Fig. 1). Recently, however, a new dynamic technique known as ramp compression has been developed, in which a sample is compressed on a timescale that is long compared to the sound-wave transit time through the sample, thus reducing dissipative processes and keeping the sample cooler than it would be in the shocked state[18]. With this technique, diamond has previously been ramp-compressed to record-high pressures (more accurately longitudinal stresses, because of the uniaxial loading) of 5 TPa at the National Ignition Facility in Livermore, California, USA[19]. This ramp data gave no indicators of a phase transformation, such as plateaus in the velocity ramp caused by changes in sound speed. A second experimental study has interpreted subtle trends in shock Hugoniot data near the melting point as evidence for the FC8–BC8–liquid triple point near 1 TPa (ref. [20]). However, neither of these studies included a measurement of structure.

In fact, whether and how diamond might transform to one of the predicted phases in a laboratory compression experiment are far from trivial questions to answer, owing to the large enthalpy barriers predicted to exist between the phases (a phenomenon that explains the very existence of ambient-pressure diamond itself, given its metastability compared with graphite). Simulations at zero Kelvin report that the predicted BC8 phase will never form under rapid compression, and the FC8 phase will persist until it becomes mechanically unstable near 3 TPa (ref. [1]). At high temperature, however, the atoms are freed to follow alternative transformation pathways and the enthalpy of formation is lower for some phases. At 2 TPa and 4,000 K FC8 is predicted to transform to the lower-energy (but still metastable) SC1 phase, and at 300 K and 2.5 TPa FC8 is predicted to transform to another metastable SC4 structure[2]. It is also predicted that BC8 will form at approximately 1 TPa, but only when released from the SC1 phase. To explore this rich

---

[1]Lawrence Livermore National Laboratory, Livermore, CA, USA. [2]Department of Physics, Clarendon Laboratory, University of Oxford, Oxford, UK. [3]Laboratory for Laser Energetics, University of Rochester, Rochester, NY, USA. [4]Departments of Mechanical Engineering, University of Rochester, Rochester, NY, USA. [5]Department of Physics and Astronomy, University of Rochester, Rochester, NY, USA. [6]University of York, Department of Physics, York, UK. ✉e-mail: lazicki1@llnl.gov

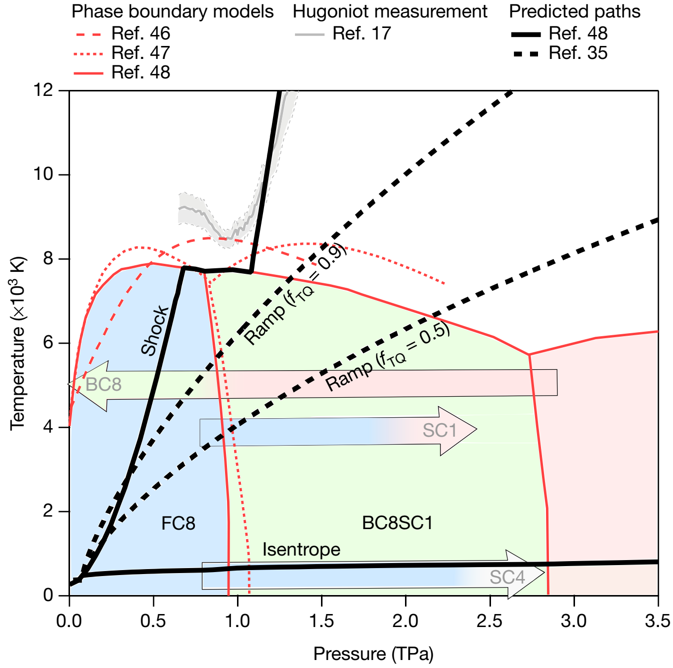

Fig. 1 | Carbon phase diagram summarizing DFT-predicted phase boundaries[45–47], Hugoniot data[17] and predicted thermodynamic paths[35,47]. The broad arrows represent the predicted structural evolution if kinetic effects are taken into account[2]. The two proposed ramp paths show the effect of different fractions of plastic work appearing as heat, described by the Taylor–Quinney factor (f_{TQ})[35]. The observation in this study of solid FC8 carbon at 2 TPa suggests that strength may be lower than predicted or that plastic work is contributing largely to microstructural changes rather than heating.

Q2

and complex landscape, it is necessary to couple the most powerful pressure drivers with in situ probes of structure.

In conjunction with dynamic ramp compression using laser ablation, quasi-monochromatic X-ray emission can be produced by irradiating separate targets at high laser intensities[21,22], and these X-rays can then be used for X-ray diffraction[23] and structural determination[24] during the nanosecond compression. We have now implemented this technique at the National Ignition Facility[25], making it possible for the first time to attempt multi-TPa measurements of structure. Here we report the results of diamond ramp-compression experiments to 2 TPa with simultaneous X-ray diffraction measurements of structure. To our knowledge, this stress state is the highest at which X-ray diffraction information has been obtained, and we find that diamond remains solid and retains the FC8 phase.

As described in the Methods, we used laser ablation to ramp compress samples of pure polycrystalline diamond or diamond-epoxy aggregates (for shots N150217 and N150927), to stress states between 0.8 TPa and 2 TPa for a duration of several nanoseconds. During the time of peak compression, separate laser beams were focused onto either germanium (Ge) or zirconium (Zr) foils offset from the diamond target, to create a bright quasi-monochromatic X-ray source with energies of 10.25 keV (Ge) or 16.25 keV (Zr). The X-rays scattered from the compressed diamond were collimated by a pinhole placed just behind the sample itself. The sample sat on the surface of a hollow container lined with image plates, such that the diffracted signal in transmission was recorded over almost a full 2π steradians, providing Debye–Scherrer diffraction patterns (Extended Data Fig. 1). On each shot the velocity history of the rear surface of the target is recorded with the Velocity Interferometer System for Any Reflector system (VISAR)[26]. A characteristics analysis is used to translate these velocity data into a stress-density history within the target[27]. The Debye–Scherrer pattern at 1.74 TPa and 2 TPa is shown in Fig. 2 (and the rest summarized in Extended Data Figs. 2 and 3) along with azimuthally averaged lineouts for all reported shots. The background subtraction algorithms and means of accurately determining the scattering angle are described in detail elsewhere[25] and illustrated in Extended Data Fig. 6. The diffraction peaks in the lineouts are fitted with a Gaussian function and the best-fit peak centroids used in a least-squares fitting to determine the density.

At 0.8 TPa the (111), (200) and (311) diffraction peaks from the FC8 structure are identifiable. As the stress increases the scattering angle for the (311) peak approaches the edge of the image plate, and between 1 TPa and 2 TPa, only the (111) and (220) peaks are reliably seen. Peak positions and deduced densities shown in Fig. 3 (summarized in Extended Data Table 1) are in good agreement with previous measurements[19,28]. In Fig. 3 we also show the angular positions at which we would expect diffraction from the BC8, SC1 and SC4 structures. None of the data

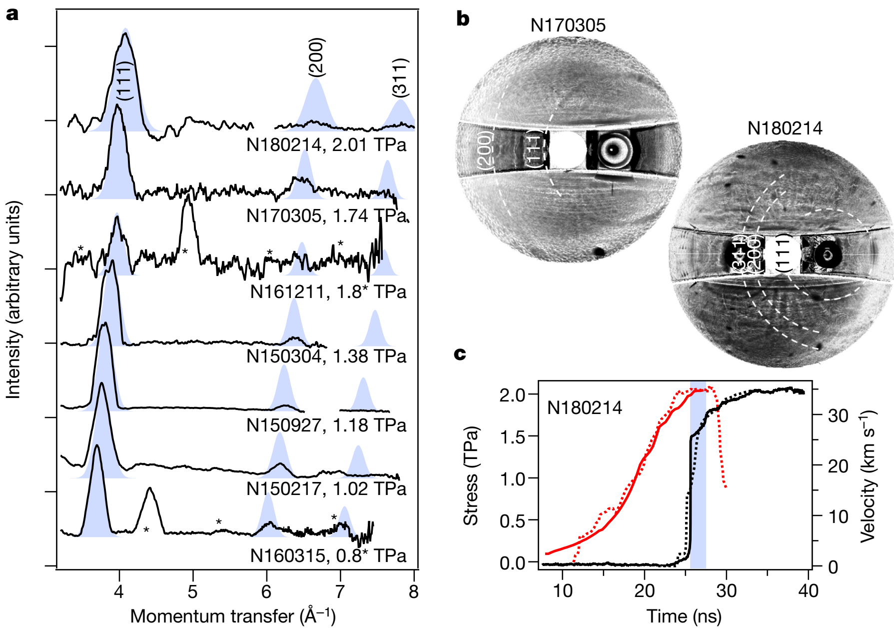

Fig. 2 | Summary of experimental data. a, X-ray diffraction lineouts (black) and ideal FC8 diffraction patterns (blue, described in Extended Data Fig. 2). Asterisks mark the position of B2 MgO diffraction peaks. Stereographic projections of the background-subtracted image plates for shots N170305 (10.25-keV X-rays) and N180214 (16.25-keV X-rays) are shown in **b**, with carbon peaks marked with white arc segments. Details of the data processing in the presence of high noise at the highest pressures is illustrated in Extended Data Figs. 6 and 7. **c**, The free-surface tamper velocity history and inferred sample pressure for shot N180214 (solid lines) agree well with radiation-hydrodynamic predictions (dashed)[48]. The compression wave is a smooth ramp within the sample and steepens to a shock by the time it reaches the measured surface. The blue band illustrates the timing of the X-ray source.

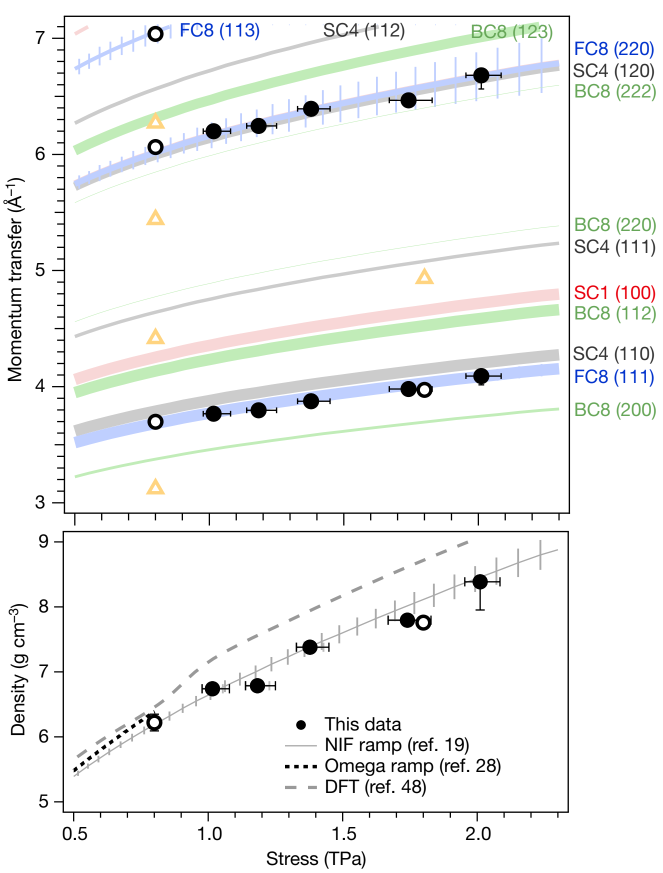

Fig. 3 | Data compared to theoretical predictions. a, Position of carbon diffraction peaks (black circles, error bars defined in the Methods section) compared with predictions for candidate phases (solid curves with widths proportional to ideal intensities normalized to the most intense peak). Diffraction from the B2 phase of MgO (yellow triangles) was observed in the two experiments. Reported stress was deduced from VISAR measurements (solid markers), or radiation-hydrodynamic simulations (open markers)[48]. The compressibility of the predicted carbon phases is taken from the National Ignition Facility experimental results[19] and the associated uncertainty is shown as error bars on the predicted FC8 lines. **b**, Inferred density from the best-fit FC8 structure, compared with the published ramp equations of state[19,28] and a DFT-based model[47]. See Methods for definition of error bars.

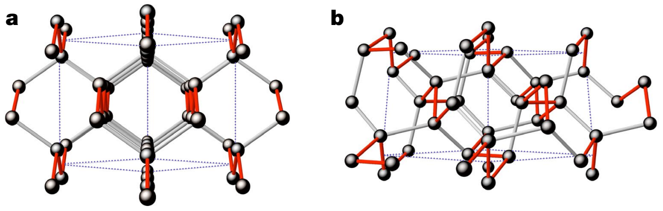

Fig. 4 | FC8 and BC8 crystal structures. Both are represented in the rhombohedral space group $\bar{R}3$ (C_2^3, number 148) with occupied 2c and 6f Wyckoff sites, which was identified as the correspondence requiring the minimum number of broken sp^3 bonds (1.5 per atom)[9]. Highlighted in red are sp^3 bonds that connect the layers. **a**, The FC8 structure with simple zigzag interlayer bonding (red) defining the {110} channels. **b**, The BC8 structure with much more complex helical interlayer bonding (red) and a lack of distinct channels.

shows evidence of these new phases. Some additional peaks (marked with asterisks) are identified with magnesium oxide (MgO; ref. [29]) in a subset of the shots where single-crystal MgO was used as a window material (see the Supplementary Information for more information).

The most likely reason we did not observe the BC8 phase is the high enthalpy barrier caused by the large number of strong sp^3 bonds that must be broken to change the structure. The FC8 and BC8 phases are shown in Fig. 4 and, although both can be viewed as layers of sp^3-bonded carbon in 6-member rings, there is no simple shift that will transform one to another. The FC8 layers are bound by zigzag interlayer bonds, which give the structure its distinctive open channels. The BC8 interlayer bonds form helical chains and adjacent layers are consequently shifted, eliminating the open channels. Mechanisms for the transformation have been suggested that require a minimum of 1.5 bonds per atom to be broken[9]; a considerable energy cost that is due to the stability of the sp^3 bond. This observation is analogous to the case of carbon's sp^3-bonded group-14 neighbours Si and Ge which, in the absence of a chemical reaction or application of substantial heat, transform to the BC8 structure only upon release from a higher-pressure phase[30,31]. Carbon's sp^3 bonds are even stronger, however, owing to the lack of *p* orbital electrons in the atomic core[12]. The predicted enthalpy barrier of around 2.5 eV per atom between FC8 and BC8[2,9] is approaching the barrier between metastable FC8 and stable graphite phases under ambient conditions, and that transformation, although spontaneous, takes geological timescales. Consequently, it may not be surprising that we do not observe the FC8-to-BC8 transition in our approximately 10-ns ramp-compression experiments. The predicted enthalpy barrier between hexagonal diamond (observed to form from shocked graphite[32]) and BC8 is lower at around 1 eV (ref. [9]), suggesting another way to seek the formation of BC8.

Not yet considered in this discussion is the role of temperature, which can open up new transformation pathways and overcome kinetic barriers. The prediction that the kinetic barrier between FC8 and metastable SC1 could be surmounted at 2 TPa and 4,000 K (ref. [2]) was potentially within our reach to test, depending on the temperature in the experiment. A lower bound on the temperature can be estimated from the heating associated with a shock to about 1 Mbar (the elastic limit of diamond[33]), which was observed on all shots, followed by an isentrope, as illustrated in Fig. 1. In the dynamic technique, however, hydrostatic conditions are approached within the sample as the shear stress is relieved by plastic flow, with an associated conversion of the plastic work to heat[18,28]. The strength of the material, which determines residual shear stress, thus strongly affects final temperature. Strength models for diamond based on DFT calculations of the elastic moduli as a function of compression[34,35] indicate that a ramp-compressed diamond sample will be well above the predicted melting temperature by 2 TPa, if we assume that most of the plastic work is converted to heat. The fact that solid X-ray diffraction is observed in this experiment at 2 TPa suggests that either the strength is lower than expected (some experimental evidence has already been put forward to indicate that diamond has a maximum resolved shear stress that is much lower than theoretical predictions[33,36]), or that a large percentage of plastic work must be accounted for some other way. This fraction of plastic work that shows up as heat, traditionally represented by the Taylor–Quinney factor (f_{TQ})[37], is usually assumed to be near 0.9 for metals, and the remainder goes towards microstructural changes like creating defects, which can be very numerous at high strain rates[38]. Within this simplified model, f_{TQ} should be nearer to 0.5 for carbon to remain solid at 2 TPa (Fig. 1)[35], if the predicted melting curve is accurate at these conditions. In reality, the evolution of lattice defects and strength in carbon along a ramp-compression pathway is likely to be complex and will certainly vary with time, and a detailed energy-budget analysis, as has been done for the case of tantalum (Ta; ref. [39]), would be fruitful.

A reliable temperature determination, which is currently lacking, would allow these data to be used directly to benchmark improved models for diamond strength, phase diagram and phase transformation kinetics under ramp conditions. These results highlight the crucial importance of developing techniques compatible with dynamic experiments for measuring temperature. Although some progress has been made by employing the Debye–Waller effect in EXAFS[40] and diffraction measurements[41], high-quality, untextured diffraction data are required, and the uncertainties in the derived values are extremely high. With the advent of high-power, high-repetition-rate lasers[42] coupled to ultrahigh-brightness free-electron-laser X-ray sources[43], it may become possible to drive diamond into the TPa pressure range and probe structure as well as temperature, using alternative techniques such as inelastic X-ray scattering[44].

Using X-ray diffraction we have here directly probed the crystal structure of diamond in the pressure regime where several phases are predicted to be more stable than the well known FC8 structure. Our data show no evidence for a phase transformation between 0.8 TPa and 2 TPa, the highest-pressure diffraction measurement ever reported. The persistence of the metastable FC8 phase up to 1 TPa beyond its predicted phase boundary gives further evidence for the extraordinary strength and stability of the carbon sp^3 bond. The observation of solid ramp-compressed diamond at 2 TPa also sets a bound for models of the melt curve, the strength and the degree of plastic work converted to heat.

Online content

Any methods, additional references, Nature Research reporting summaries, source data, extended data, supplementary information, acknowledgements, peer review information; details of author contributions and competing interests; and statements of data and code availability are available at https://doi.org/10.1038/s41586-020-03140-4.

1. Scandolo, S., Chiarotti, G. L. & Tosatti, E. SC4: a metallic phase of carbon at terapascal pressures. *Phys. Rev. B* **53**, 5051–5054 (1996).
2. Sun, J., Klug, D. D. & Martoňák, R. Structural transformations in carbon under extreme pressure: beyond diamond. *J. Chem. Phys*. **130**, 194512 (2009).
3. Martinez-Canales, M., Pickard, C. J. & Needs, R. J. Thermodynamically stable phases of carbon at multiterapascal pressures. *Phys. Rev. Lett*. **108**, 045704 (2012).
4. Madhusudhan, N., Lee, K. K. M. & Mousis, O. A possible carbon-rich interior in super-earth 55 Cancri e. *Astrophys. J*. **759**, L40 (2012).
5. Mashian, N. & Loeb, A. CEMP stars: possible hosts to carbon planets in the early universe. *Mon. Not. R. Astron. Soc*. **460**, 2482–2491 (2016).
6. Frondel, C. & Marvin, U. B. Lonsdaleite, a hexagonal polymorph of diamond. *Nature* **214**, 587–589 (1967).
7. Narayan, J. & Bhaumik, A. Novel phase of carbon, ferromagnetism, and conversion into diamond. *J. Appl. Phys*. **118**, 215303 (2015).
8. Johnston, R. L. & Hoffmann, R. Superdense carbon, C8: supercubane or analog of γ-silicon? *J. Am. Chem. Soc*. **111**, 810–819 (1989).
9. Mailhiot, C. & McMahan, A. K. Atmospheric-pressure stability of energetic phases of carbon. *Phys. Rev. B* **44**, 11578–11591 (1991).
10. Oganov, A. R. & Glass, C. W. Crystal structure prediction using ab initio evolutionary techniques: principles and applications. *J. Chem. Phys*. **124**, 244704 (2006).
11. Oganov, A. R., Hemley, R. J., Hazen, R. M. & Jones, A. P. Structure, bonding, and mineralogy of carbon at extreme conditions. *Rev. Mineral. Geochem*. **75**, 47–77 (2013).
12. Yin, M. T. & Cohen, M. L. Will diamond transform under megabar pressures? *Phys. Rev. Lett*. **50**, 2006–2009 (1983).
13. Biswas, R. & Martin, R. M., Needs, R. J. & Nielsen, O. H. Stability and electronic proper- ties of complex structures of silicon and carbon under pressure: density-functional calculations. *Phys. Rev. B* **35**, 9559–9568 (1987).
14. Fahy, S. & Louie, S. G. High-pressure structural and electronic properties of carbon. *Phys. Rev. B* **36**, 3373–3385 (1987).
15. Dubrovinsky, L., Dubrovinskaia, N., Prakapenka, V. B. & Abakumov, A. M. Implementation of micro-ball nanodiamond anvils for high-pressure studies above 6 Mbar. *Nat. Commun*. **3**, 1163 (2012).
16. Wu, H., Luo, X., Wen, L., Sun, H. & Chen, C. Extreme static compression of carbon to terapascal pressures. *Carbon* **144**, 161–170 (2019).
17. Eggert, J. H. et al. Melting temperature of diamond at ultrahigh pressure. *Nat. Phys*. **6**, 40–43 (2010).
18. Swift, D. C. Numerical solution of shock and ramp compression for general material properties. *J. Appl. Phys*. **104**, 073536 (2008).
19. Smith, R. F. et al. Ramp compression of diamond to five terapascals. *Nature* **511**, 330–333 (2014).
20. Knudson, M. D., Desjarlais, M. P. & Dolan, D. H. Shock-wave exploration of the high-pressure phases of carbon. *Science* **322**, 1822–1825 (2008).
21. Barrios, M. A. et al. X-ray area backlighter development at the National Ignition Facility. *Rev. Sci. Instrum*. **85**, 11D502 (2014).
22. Coppari, F. et al. Optimized x-ray sources for x-ray diffraction measurements at the Omega Laser Facility. *Rev. Sci. Instrum*. **90**, 125113 (2019).
23. Wark, J. S., Whitlock, R. R., Hauer, A. A., Swain, J. E. & Solone, P. J. Subnanosecond x-ray diffraction from laser-shocked crystals. *Phys. Rev. B* **40**, 5705–5714 (1989).
24. Rygg, J. R. et al. Powder diffraction from solids in the terapascal regime. *Rev. Sci. Instrum*. **83**, 113904 (2012).
25. Rygg, J. R. et al. X-ray diffraction at the National Ignition Facility. *Rev. Sci. Instrum*. **91**, 043902 (2020).
26. Celliers, P. M. et al. Line-imaging velocimeter for shock diagnostics at the OMEGA laser facility. *Rev. Sci. Instrum*. **75**, 4916–4929 (2004).
27. Rothman, S. D. et al. Measurement of the principal isentropes of lead and lead–antimony alloy to ~400 kbar by quasi-isentropic compression. *J. Phys. D* **38**, 733–740 (2005).
28. Bradley, D. K. et al. Diamond at 800 GPa. *Phys. Rev. Lett*. **102**, 075503 (2009).
29. Coppari, F. et al. Experimental evidence for a phase transition in magnesium oxide at exoplanet pressures. *Nat. Geosci*. **6**, 926–929 (2013).
30. Nelmes, R. J., McMahon, M. I., Wright, N. G., Allan, D. R. & Loveday, J. S. Stability and crystal structure of BC8 germanium. *Phys. Rev. B* **48**, 9883–9886 (1993).
31. Kurakevych, O. O. et al. Synthesis of bulk BC8 silicon allotrope by direct transformation and reduced-pressure chemical pathways. *Inorg. Chem*. **55**, 8943–8950 (2016).
32. Turneaure, S. J., Sharma, S. M., Volz, T. J., Winey, J. M. & Gupta, Y. M. Transformation of shock-compressed graphite to hexagonal diamond in nanoseconds. *Sci. Adv*. **3**, eaao3561 (2017).
33. McWilliams, R. S. et al. Strength effects in diamond under shock compression from 0.1 to 1 TPa. *Phys. Rev. B* **81**, 014111 (2010).
34. Orlikowski, D., Correa, A. A., Schwegler, E. & Klepeis, J. E. A Steinberg-Guinan model for high-pressure carbon: diamond phase. *AIP Conf. Proc*. **955**, 247–250 (2007).
35. Swift, D. C. et al. Equation of state and strength of diamond in high pressure ramp loading. Preprint at https://arxiv.org/abs/2004.03071 (2020).
36. Lang, J. M., Winey, J. M. & Gupta, Y. M. Strength and deformation of shocked diamond single crystals: orientation dependence. *Phys. Rev. B* **97**, 104106 (2018).
37. Taylor, G. I. & Quinney, H. The latent energy remaining in a metal after cold working. *Proc. R. Soc. Lond. A* **143**, 307–326 (1934).
38. Suggit, M. J. et al. Nanosecond white-light Laue diffraction measurements of dislocation microstructure in shock-compressed single-crystal copper. *Nat. Commun*. **3**, 1224 (2012).
39. Heighway, P. G. et al. Nonisentropic release of a shocked solid. *Phys. Rev. Lett*. **123**, 245501 (2019).
40. Ping, Y. et al. Solid iron compressed up to 560 GPa. *Phys. Rev. Lett*. **111**, 065501 (2013).
41. Murphy, W. J., Higginbotham, A., Wark, J. S. & Park, N. Molecular dynamics simulations of the Debye-Waller effect in shocked copper. *Phys. Rev. B* **78**, 014109 (2008).
42. Ertel, K. et al. DiPOLE: A scalable laser architecture for pumping multi-Hz PW systems. *Proc. SPIE* **8780**, 288–292 (2013).
43. Pellegrini, C. X-ray free-electron lasers: from dreams to reality. *Phys. Scr*. **T169**, 014004 (2016).
44. McBride, E. E. et al. Setup for meV-resolution inelastic x-ray scattering measurements and x-ray diffraction at the matter in extreme conditions endstation at the Linac Coherent Light Source. *Rev. Sci. Instrum*. **89**, 10F104 (2018)
45. Wang, X., Scandolo, S. & Car, R. Carbon phase diagram from ab initio molecular dynamics. *Phys. Rev. Lett*. **95**, 185701 (2005).
46. Correa, A. A., Bonev, S. A. & Galli, G. Carbon under extreme conditions: phase boundaries and electronic properties from first-principles theory. *Proc. Natl Acad. Sci. USA* **103**, 1204–1208 (2006).
47. Benedict, L. X. et al. Multiphase equation of state for carbon addressing high pressures and temperatures. *Phys. Rev. B* **89**, 224109 (2014).
48. Zimmerman, G., Kershaw, D., Bailey, D. & Harte, J. LASNEX code for inertial confinement fusion. *J. Opt. Soc. Am*. **68**, 549 (1978).

Q8

Methods

Target details

Materials, part thicknesses and assembly are shown in Extended Data Table 1 and Fig. 1. We used two types of diamond samples for this study: ~50-µm-thick layers of monocrystalline diamond powder embedded in epoxy, and 30–100-µm-thick plates of microcrystalline diamond. The diamond-epoxy composite targets had a packing fraction of 0.53 diamond, approaching the maximally random jammed packing fraction of 0.64. The diamond was a monocrystalline powder with grain size between 50 nm and 100 nm, and the epoxy was Stycast 1266, vacuum-outgassed before mixing.

There is a large impedance mismatch between diamond and epoxy, meaning that the compression wave will drop to a much lower pressure when it passes from diamond to epoxy, sending a release wave back into the diamond. However, with grain sizes of 50–100 nm and sound speeds of at least 3 km s^{-1}, the pressure in a grain will equilibrate with the neighbouring diamond grains in about 30 ps or less; much faster than the duration of the 25-ns ramp pulse, and the sample pressure and density will evolve along or very close to the same path as the full-density diamond. The motivation for using a slurry rather than full-density diamond sample was based on the expectation, from available strength models and from some experimental efforts on the Omega laser facility (The Laboratory for Laser Energetics at the University of Rochester, New York, USA) that plastic work heating would cause the diamond ramp to cross the melting line by 8–12 Mbar. The epoxy was intended to reduce the deviatoric stress imposed on the diamond, and also to allow heat to rapidly conduct away from the diamond. The actual effect of the presence of epoxy on the sample temperature depends on the thermal conductivity, which is not well known under these conditions. In the limit of zero conductivity, the diamond temperature will be at most that of full-density diamond. In the limit of infinite conductivity, the temperature rise may follow a path similar to an isentrope in the epoxy, which can be estimated using an equation of state model. The SESAME 7603 model equation of state[49] suggests that the temperature may reach 2,500 K by 1.2 TPa, lower than the predicted temperature of the full-density diamond (Fig. 1). As it became necessary to maximize the diamond volume in order to increase the diffraction signal above the increasing drive background at the highest stresses, we experimented with full-density microcrystalline diamond samples. We found that the samples did not in fact melt as expected, and the slurry target style was subsequently abandoned.

The microcrystalline diamond samples were prepared by Diamond Materials GmbH using chemical vapour deposition. The ambient material has large (>1 µm) grain sizes and a 110 fibre texture[50].

The sample was sandwiched between an ablator package towards the laser drive and a tamper towards the diagnostic. The ablator is composed of a beryllium plate, which the lasers irradiate to generate the pressure drive. The laser ablation also generates a broad spectrum of low-energy X-rays peaking around 2 keV. Unshielded, these X-rays heat the diamond sample before compression, and also contribute to a high image plate background. A layer of absorbing material (gold (Au) or Zr) is therefore sandwiched between the ablator and the diamond sample to absorb these X-rays. A single-crystal diamond or MgO plate is positioned on the other side of the sample functions to delay the arrival of waves that originate at the vacuum interface and drop the pressure to zero.

Laser configuration

The experiments were performed at the National Ignition Facility. Samples were compressed up to 2 TPa using 16 laser beams with their pulses shaped to ramp the total laser intensity from 0 to as high as 500 TW cm^{-2} over 25–30 ns (Extended Data Fig. 4). The beam profiles were smoothed using continuous phase plates with approximately 1-mm circular profiles, which were further smoothed using spectral dispersion and orthogonal polarization. The peak laser intensity was maintained for about 5 ns, while a 2-ns-long burst of quasi-monochromatic X-rays illuminated the compressed sample and was diffracted onto image plates. The X-rays were generated by irradiating a foil of Ge or Zr, placed about 32 mm from the sample, with up to 24 laser beams at an intensity of about 7.5×10^{15} W cm^{-2}. The lasers ionize the metal and helium-like emission lines are generated into 4π from the plasma, with energies of 10.25 keV (Ge) or 16.19 keV (Zr), with a 1% bandwidth owing to two main transitions being present ($1s2p\ ^1\mathrm{P}$ to $1s^2\,^1\mathrm{S}$, and $1s2p\ ^3\mathrm{P}$ to $1s^2\,^1\mathrm{S}$)[21]. The X-ray fluence at the sample is about 30×10^{18} photons per m^2. X-rays that scatter off the sample are collimated by a 400-µm-diameter pinhole made of a uranium–6 wt% niobium alloy placed behind the sample.

Stress state determination

The stress state reached in the samples is determined by measuring the velocity of the free surface of the diamond tamper using the VISAR velocimetry diagnostic[26]. For shots below 1.5 TPa, etalons with sensitivity of 3.1251 km s^{-1} per fringe and 5.4603 km s^{-1} per fringe were used and at higher pressure a combination of 13.64 km s^{-1} per fringe and 5.4603 km s^{-1} per fringe was used. Free-surface velocities for the shots reported here, which used a diamond tamper, are shown in Extended Data Fig. 5. In all shots the sample is initially shocked to 0.1 TPa, which is the elastic limit of diamond, and then ramp compressed. By the time the compression wave reaches the free surface, the ramp has partially steepened into a shock, as predicted by the radiation-hydrodynamic simulations (Extended Data Fig. 5c). The diamond equation of state along a ramp-compression pathway is well known from previous experiments[19,28], so the stress history across the bulk of the sample can be inferred from this velocity using the method of characteristics[27].

Stress uncertainty

Uncertainty in the stress state of the sample at the time of the experiment comes from several sources, as follows. (1) Uncertainty in the diamond free surface velocity measurement due to spatial variation across the sample and to a velocity resolution of 3% of the velocity per fringe. These combined sources contributed between 0.015–0.040 TPa to the uncertainty from shot to shot. (2) Uncertainty in the diamond equation of state used to perform the characteristics analysis. The data shown in this report was analysed using the ramp equation of state measured for full-density diamond up to 0.8 TPa (ref. [28]), extrapolated to the 2-TPa range by assuming a linear relationship between the longitudinal sound speed and particle velocity. The error in the diamond ramp equation of state was also extrapolated to 20 Mbar and propagated, contributing 3.5% to the stress uncertainty reported here. The choice of ramp equation of state is a systematic uncertainty that is not explicitly included in the error bar. If the 5-TPa ramp equation of state measured for nanocrystalline diamond[19] is used, the resulting stresses are systematically lower (by up to 0.04 TPa) near 1 TPa, and within 0.005–0.01 TPa near 2 TPa, because of the similarity in sound speed at those conditions. (3) Uncertainty in the strength of diamond, which introduces a systematic error in the characteristics analysis. The analysis method assumes that the pressure releases along the same pathway as the compression, ignoring any change in strength. A test with radiation-hydrodynamic simulations suggests that this assumption could result in an underestimate of the stress of the order of 0.05 TPa (Extended Data Fig. 5b). We have consequently added a 0.05-TPa contribution to the higher-stress error bar. (4) Uncertainty in the timing of the X-ray source due to the timing accuracy of the streak camera diagnostic that registered it, and to the finite rise and decay times of the X-ray emission, which contributed between 0.002 TPa and 0.01 TPa to the total uncertainty. There is also a contribution from the uncertainty in the target layer thicknesses that is due to the accuracy of the metrology and to the variation in thickness across the part. This turned out to be negligible, since the metrology accuracy is <0.5 µm, and the diamond parts are very flat (<0.5 μm variation across the region probed in the experiment).

There is a spread of stress states in the sample over the duration of the X-ray pulse that varies from shot to shot, depending on how accurately the X-ray source was timed. Stresses reported here are the mean of a histogram of those stress states. Normally we consider that the width of this histogram is correlated with the (symmetric) width of the X-ray diffraction peaks and does not contribute to the stress uncertainty. In this case, however, because there is some uncertainty as to which region of the thick sample is contributing to the diffraction pattern, the histogram width may actually be correlated with an additional source of uncertainty. It is unclear how to include this contribution accurately in our error bar, so we summarize the full-width at half-maximum (FWHM) of the histogram of stress states across the sample, over the duration of the X-ray source pulse, in Extended Data Table 1.

X-ray diffraction measurement

The TARDIS (TARget Diffraction In-Situ) X-ray diffraction diagnostic[25] is a half-cylinder-shaped chamber made of thick Ta–tungsten alloy, lined with three image plates. The metal foil used for the X-ray source is mounted to an arm attached to the front of the diagnostic. The sample and collimating pinhole are mounted on the front of the chamber and an aperture to allow entrance of the VISAR laser used for the velocity measurement is positioned on the opposite wall (Extended Data Fig. 1). Filter materials are layered on the image plates inside the chamber, to absorb unwanted low- and high-energy X-rays. 5–15-μm-thick layers of Ge or Zr (material chosen to match the X-ray source, since their helium-like emission-line (He_α) energies fall below their absorption edges) are the primary filters, and in several shots an additional 75–150-μm thickness of Al is added, to further block the low-energy ablation plasma X-rays. 10-μm-thick and 15-μm-thick Ge filters are made by depositing 5 μm of Ge onto 25-μm-thick layers of kapton, and stacking multiples to make up the full thickness. A 500-μm-thick rigid polycarbonate shell is made to fit into the TARDIS diagnostic box, supporting the filter layers and housing a thick Ta canister around the direct X-ray beam, to attenuate it so that it does not overly saturate the image plate, and to block scattered X-rays and fluorescence that it generates.

After the shot the diagnostic is retrieved, disassembled and image plates scanned. The quasi-monochromatic X-ray scattering from the sample is time-resolved because of the duration of the X-ray pulse, but the image plate data are time-integrated so it registers all scattered X-rays from the ablation plasma (as well as Bremsstrahlung radiation from the X-ray source and subsequent fluorescence), which occur over the course of the experiment and may penetrate the filtering. For the high drive intensities necessary to achieve 2-TPa pressures, the ablation plasma background on the image plates is extreme (Extended Data Fig. 4b), and good background subtraction methods are therefore critical. We have used the sensitive nonlinear iterative peak (SNIP) method presented in detail by Rygg et al.[25] and it is shown applied to one of the high-pressure shots in Extended Data Fig. 6. In addition to a smoothly varying background from the broadband radiation through the pinhole, there are many additional sources for spurious features in the image plates, which compete with the Bragg scattering. An example is shown in Extended Data Fig. 7.

Structure uncertainty

The uncertainty in diffraction peak angles due to image plate calibration is 0.2°, as described elsewhere[25]. Uncertainty in the peak centroid location from peak fitting is negligible for the (111) peak (0.01°) but is near 0.1° for the (220) peak, which rises barely above the noise, in several cases. We consider an additional source of uncertainty based on the fact that there is a large thickness of diamond material (pusher, sample, tamper) in the target that may contribute to the X-ray diffraction signal. We do not rule out that some of this diamond material may be melted, either owing to heating from the drive on the side closest to the laser, or owing to shocks forming on the side closer to the diagnostic. Additionally, scattering from the diamond window has an outsize contribution to the average intensity in some cases because of the strong texture in the crystal. This large potential sample volume and uncertainty as to which part contributes most substantially to the diffraction signal means that we consider a range of possible distances between the sample and the detector, which has an impact on the calibration. This introduces an angle-dependent uncertainty of 0.05° for the (111) peak and 0.2° for the (220) peak. There is an additional source of uncertainty for shot N180214 because this shot used a Zr X-ray source, and it reflects the fact that the precise X-ray source energy is not well known. The reported numbers assume an X-ray energy of 16.25 keV, which is the average of the two Zr helium-like emission lines, as is done for the case of Ge. However, there is some evidence that the Zr is not being fully ionized to the He-like emission so the energy may be peaked lower; nearer to 16 keV (C. Krauland, private communication). We represent this uncertainty with an asymmetric error bar. A rigorous assessment of uncertainty in peak angles is necessary to rule out other candidate structures (Extended Data Fig. 8). The same sources of uncertainty are reflected in the density error bars, which also include the error in the least-squares fitting of the diffraction peaks to the FC8 structure.

MgO diffraction

Single-crystal MgO was used as a window material on a subset of the shots, and in these cases extra peaks were observed in the diffraction patterns at positions consistent with the high pressure B2 phase of MgO (Extended Data Fig. 2a, e). Above the phase transformation the single-crystal window MgO breaks apart, resulting in powder-like diffraction peaks and causing the window transmission to drop substantially (Extended Data Fig. 9a, b). In addition to the drop in VISAR visibility, the ramp equation of state (needed for the characteristics analysis) and index of refraction (used to perform a correction to the VISAR data) of MgO are not well known under these conditions, so the stress cannot be determined with accuracy and must be inferred from radiation-hydrodynamic simulations[48]. These simulations (Extended Data Fig. 9c), show that, at the time of the experiment (that is, the duration of the X-ray source), 1/3 to 1/2 of the MgO window is in a uniform stress state at equilibrium with the diamond window, and the remaining volume is experiencing a strong stress gradient in which no single volume will diffract with sufficient intensity. We therefore report the peak positions in Extended Data Fig. 9d at the same stress as the diamond sample. These results are consistent with the high-pressure B2 phase that was reported by ref. [29]. The earlier diffraction study at the smaller-scale Omega laser facility was limited to shorter ramp drives (and thus, smaller sample volumes), and fewer photons in the X-ray source, so only a single diffraction peak was registered. Near 0.8 TPa we record 4–5 diffraction peaks with the right spacing and relative intensities to enable us to unambiguously identify this phase as B2 MgO and exclude the possibility that it originates from the diamond. The distinctive texture of the B2 MgO diffraction is consistent with the observations in a study of shocked MgO (J. K. Wicks et al. Combined temperature, structure, and density measurement of phase transitions of MgO along the Hugoniot to 634 GPa; manuscript in preparation) and will be explored in more detail in a future publication. By 1.8 TPa (stress again inferred from the simulations) the background levels are close to overwhelming the signal and again we see only a single peak, but the angle is consistent with the strongest peak of B2 MgO, suggesting that this phase persists.

Data availability

The source data shown in the figures are provided, where not already summarized in Extended Data Table 1. Additional data are available from the corresponding author upon request. Source data are provided with this paper.

Code availability

The data analysis code is available at https://github.com/HEXRD.

49. Boettger, J. C. *SESAME Equation Of State For Epoxy*. Report LA-12755-MS (Los Alamos National Laboratory, 1994).
50. Wild, Ch., Herres, N. & Koidl, P. Texture formation in polycrystalline diamond films. *J. Appl. Phys*. **68**, 973–978 (1990).
51. Vedam, K. & Schmidt, E. D. D. Variation of refractive index of MgO with pressure to 7 kbar. *Phys. Rev*. **146**, 548–554 (1966).
52. Lazicki, A. et al. X-ray diffraction of solid tin to 1.2 TPa. *Phys. Rev. Lett*. **115**, 075502 (2015).

Acknowledgements We acknowledge discussions with B. Remington, M. Millot and D. Klug, and we thank the National Ignition Facility staff and the National Ignition Facility Discovery Science programme. This work was performed under the auspices of the US Department of Energy by Lawrence Livermore National Laboratory under contract number DE-AC52-07NA27344. J.S.W. thanks the UK EPSRC for support under grants EP/J017256/1 and EP/S025065/1. D.McG. was supported by LLNS under contract number B595954.

Author contributions J.S.W. and J.H.E. conceived the work. A.L., D.McG., J.R.R., R.F.S., M.G.G., P.G.H., A.H. and M.J.S. performed the experiments. D.G.B. designed the laser pulse shapes. A.L. analysed the data with assistance from J.R.R., J.H.E., D.E.F., D.E. and J.V.B. D.C.S., F.C., C.E.W., R.G.K., J.M.McN., R.E.R. and G.W.C. contributed to the design of the work and interpretation of the data. A.L. and J.S.W. wrote the paper. All coauthors commented critically on the manuscript.

Competing interests The authors declare no competing interests.

Additional information

Supplementary information The online version contains supplementary material available at https://doi.org/10.1038/s41586-020-03140-4.

Correspondence and requests for materials should be addressed to A.L.

Peer review information *Nature* thanks Philip Dalladay-Simpson and the other, anonymous, reviewer(s) for their contribution to the peer review of this work. Peer reviewer reports are available.

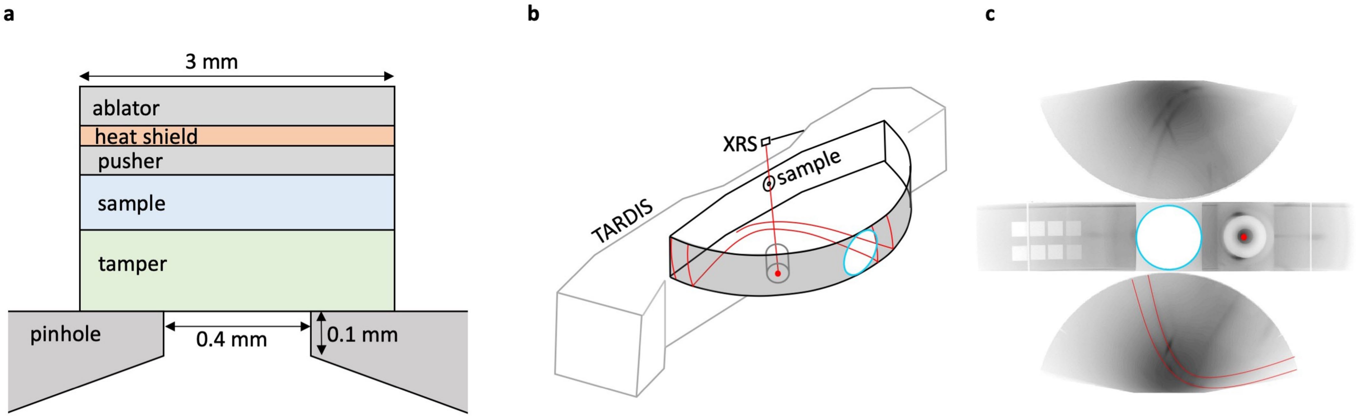

Extended Data Fig. 1 | Experimental configuration. a, Cross-section of diffraction sample: a description of the sample layers for each shot is shown in Extended Data Table 1. **b**, TARDIS diagnostic geometry with X-ray source (XRS) beam and scattered Bragg peaks on the image plate illustrated by red lines. **c**, Raw data scans of the three TARDIS image plates for shot N160315.

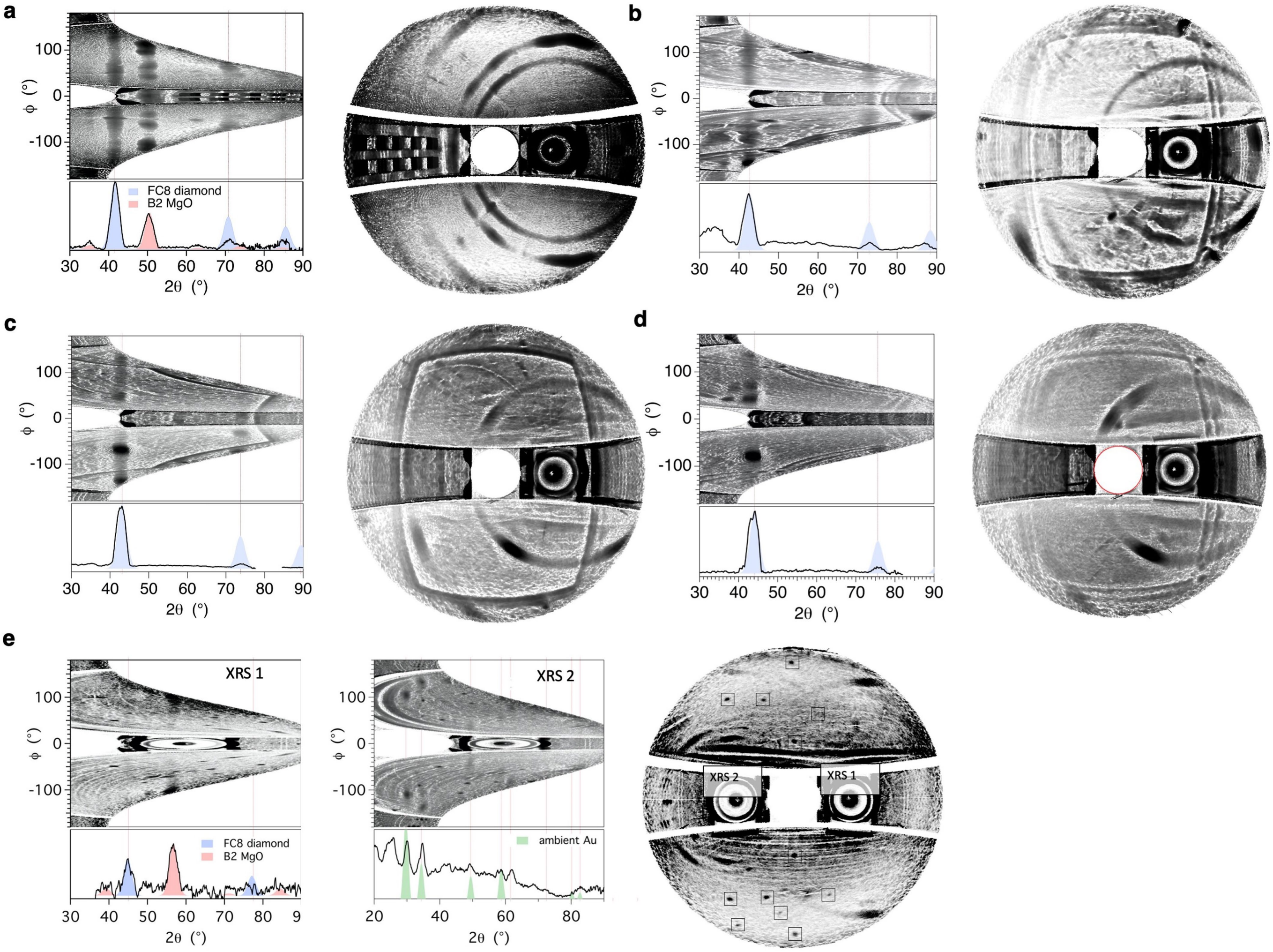

Extended Data Fig. 2 | Summary of reported X-ray diffraction data. Image plates are background-subtracted and projected into azimuthal angle ϕ versus 2θ and stereographic space. The circular opening at the centre is a hole in the diagnostic through which the VISAR laser can pass. **a**, N160315 (about 0.8 TPa) has diffraction peaks from the FC8 sample and B2 MgO window. The model ideal diffraction pattern includes the structure factor, multiplicity, Lorentz polarization factor (for a flat powder sample in transmission), and an instrument broadening tuned to match the data (the peak widths are proportional to the spatial extent of the emitting plasma cloud around the X-ray source, which varies somewhat from shot to shot). The peak width FWHM is between 1° and 1.5°, which is consistent with our source size and typical shot-to-shot variation. We do not attempt to model the effects of texture or temperature, which are both important in this data. The high temperatures are primarily responsible for the intensity mismatch between the real and ideal diffraction data at high angle, owing to the Debye–Waller effect. The square-shaped features on the rectangular plate are an array of Ross-pair filters designed to constrain the spectrum of the background radiation. **b**, N150217 (1.02 TPa): two peaks consistent with the FC8 structure are evident (ideal pattern shown in blue). The large double rectangular feature centred on the VISAR hole (also seen in **c** and **d**) is a pinhole image of a region at the front of the TARDIS box that generates fluorescence when illuminated by the hard X-rays and fast electrons coming from the X-ray source. The diagnostic was redesigned after 2015 to eliminate this feature. The smaller rectangular feature centred around the direct beam spot (also seen in **c** and **d**) is a combination of fluorescence from the front face of a cylindrical shield positioned around the direct beam spot, to block image plate fluorescence, and the shadow of the fixturing holding the shield in place. The design of this shield was also subsequently improved. **c**, N150927 (1.18 TPa): in this shot there is evident overlap between the polycrystalline diamond diffraction, which shows up as continuous rings, and strongly textured diffraction from the single-crystal diamond windows. **d**, N150304 (1.38 TPa). **e**, N161211 (about 1.8 TPa). In this shot, two spatially and temporally separated X-ray sources were used to yield two separate, easily distinguishable ring patterns, for the purpose of improving image plate calibration (the first pattern is from the undriven target and primarily picks up the scattering from the undriven Au heat shield). On this shot there is also a pattern of Laue spots evident on the image plates because the X-ray source has a broad, high-energy Bremsstrahlung tail that scatters off the windows, which are still undriven single crystals during the earlier X-ray exposure. Laue spots consistent with scattering of 5–25 keV radiation from {001}-oriented single crystal MgO are marked with black squares.

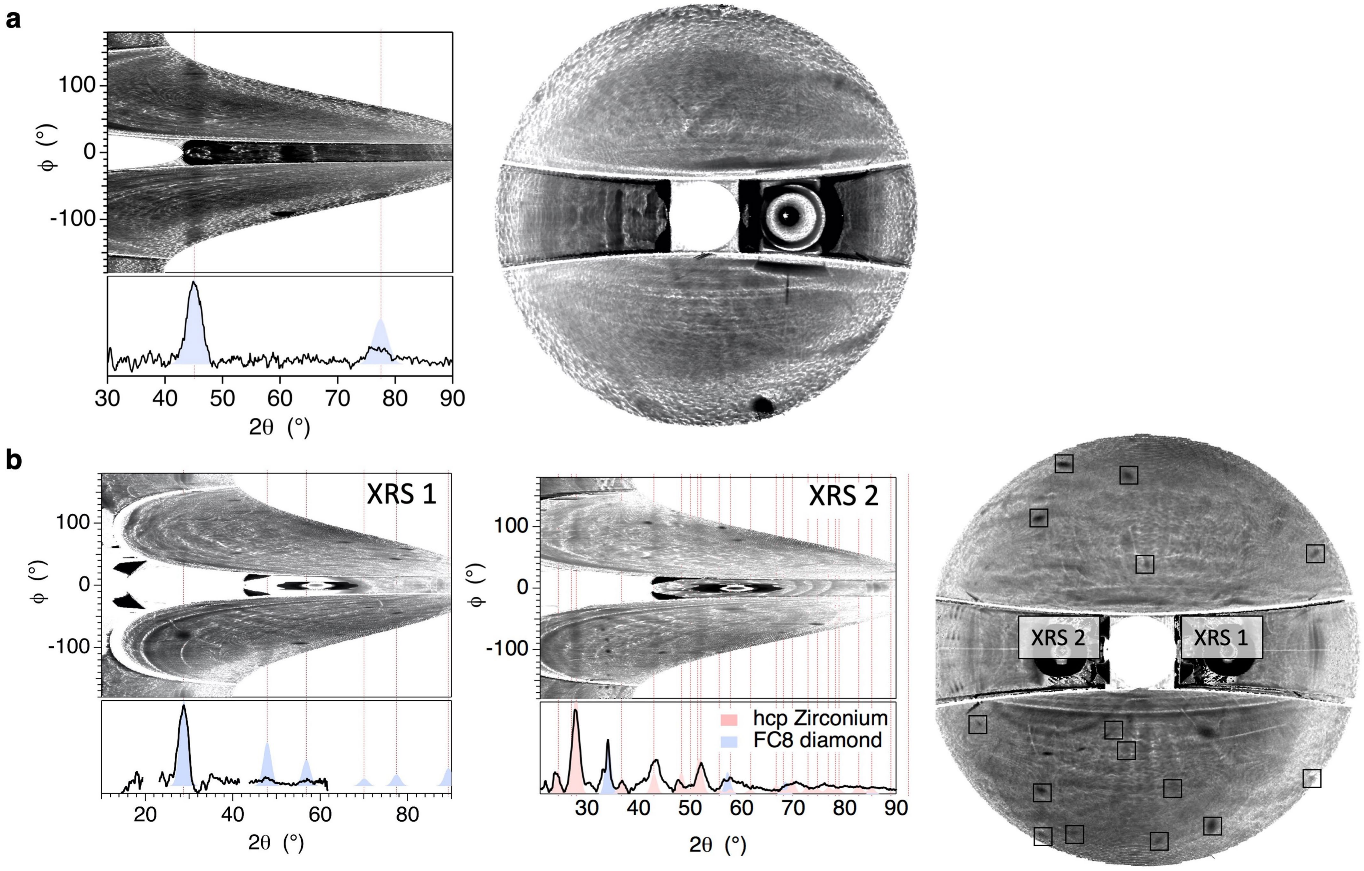

Extended Data Fig. 3 | Summary of reported X-ray diffraction data. **a**, N170304 (1.74 TPa): two peaks consistent with the FC8 structure are evident. **b**, N180214 (2.01 TPa): 2–3 peaks consistent with the FC8 structure are evident. The background is so high on this shot that diffraction is observed only when the single-crystal-like texture allows it to arise above the background, as is the case for the (111) peak, or the peak falls in a region of the image plate partially shielded from the ablation plasma background by the pinhole (further explained in Extended Data Fig. 7). This shot used a Zr (16.25 keV) X-ray source to measure diffraction at peak compression (XRS 1), so all peaks appear at lower angles compared to the rest of the shots with Ge (10.25 keV) X-ray sources. The second X-ray source (XRS 2) was Ge, and was fired before the compression wave entered the target, to capture diffraction from uncompressed hexagonal close-packed (hcp) Zr and FC8 diamond. These additional diffraction lines were used to improve the image plate angular calibration. The broadband Bremsstrahlung tail of the Ge X-ray source scattered off the uncompressed single-crystal diamond window to produce the Laue spots, marked with black squares in the stereographic projection. These positions are consistent with scattering from a {110}-oriented crystal, with an energy spanning 15–35 keV.

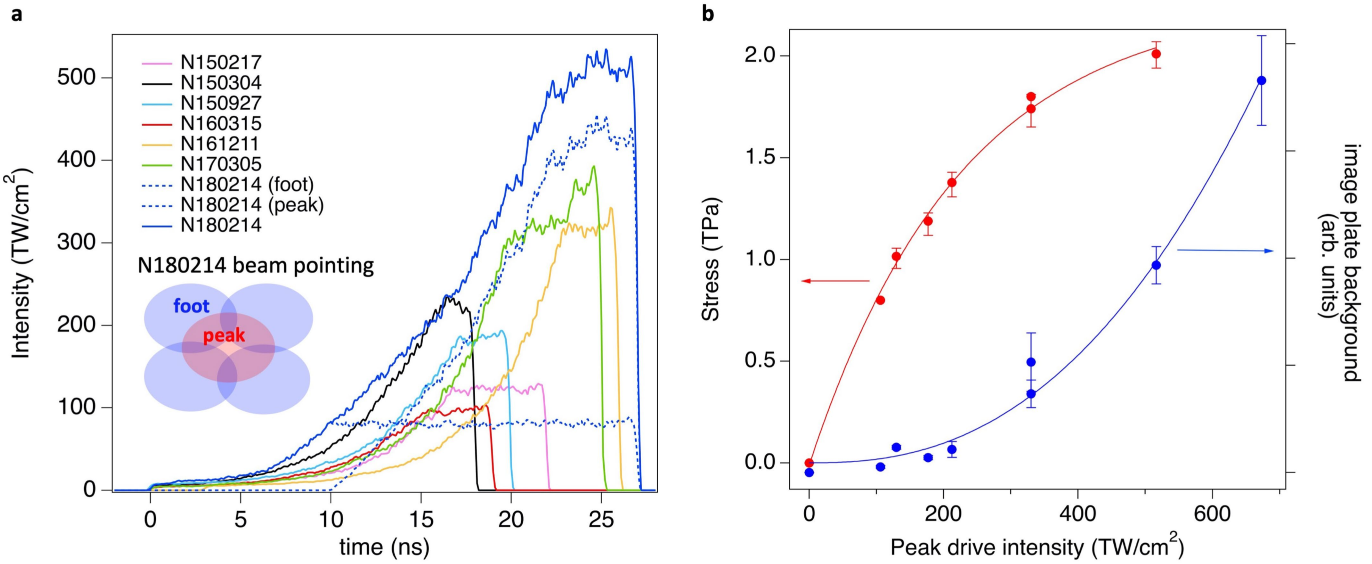

Extended Data Fig. 4 | Laser drive intensities and their relationship to sample stress and image plate background. a, The sample drive for all but the highest-stress shot N180214 used 16 overlapped beams at the National Ignition Facility with phase plates to produce a 0.9 mm × 1.2 mm elliptical spot when projected onto the sample. The transverse uniformity of the stress in the sample degrades with increasing stress. By 1.8 TPa, two-dimensional radiation-hydrodynamic simulations predict that the uniformity is still within 5% out to a radius of 400 μm but at the highest stress it becomes necessary to delay the lateral release waves by increasing the area of the drive initially. To accomplish this, we tile 8 of the beams to form an approximately uniform 1.8 mm × 1.8 mm square drive spot and use these beams to drive the sample to near 0.8 TPa, after which we drive to 2 TPa using 8 overlapped beams (cartoon inset). With this drive, simulations indicate that the stress is uniform to within 5% out to a radius of 300 μm and drops an additional 2–3% by a radius of 400 μm. The maximum sample radius for which an unobstructed ray may pass through the pinhole aperture is about 330 μm by peak compression (the sample has moved 200 μm closer to the aperture), so this transverse uniformity is adequate. For the highest power laser drives, high background levels on the image plates coming from X-rays produced in the laser-ablation process nearly overwhelm the X-ray diffraction data, and subsequent attempts to measure diffraction above 2 TPa were unsuccessful for that reason. The difficulty of achieving stresses of 2 TPa and higher is illustrated in **b**. The longitudinal stress produced from a given drive intensity increases in a sublinear fashion, while the increase in background from the ablation plasma is strongly superlinear. Image plate backgrounds shown in this figure were taken from the same regions on the image plate in each shot and were normalized by the relative transmission through the different sample and filter materials and thicknesses.

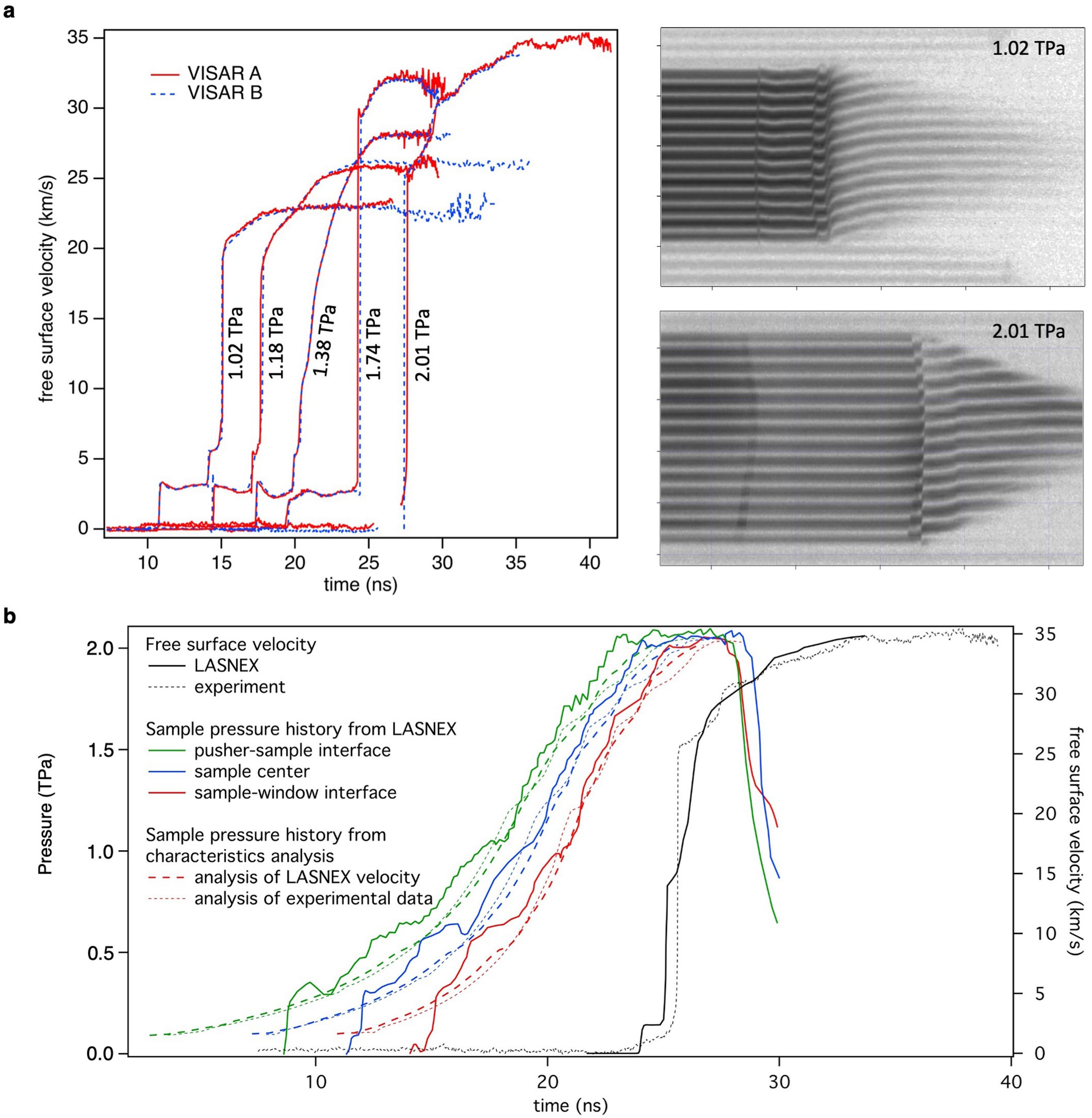

Extended Data Fig. 5 | VISAR summary and pressure inference. a, VISAR velocity histories showing the velocity of the rear surface of the diamond window. In all cases the diamond elastic wave shocks the samples to an initial ~0.1 TPa before subsequent slower compression. By 2 TPa, the elastic wave is nearly overtaken by a strong growing shock that forms within the rear diamond tamper. **b**, Experimental diamond window free-surface velocity measurement and stress histories in the diamond sample inferred from characteristics analysis, compared to the LASNEX radiation-hydrodynamic code predictions for shot N180214 (2.01 TPa). To achieve reasonable agreement with experimental breakout times and peak velocities, it was necessary in the simulation to turn off diamond strength in the sample and window after the elastic wave had reached the free surface. The characteristics method was also used to infer stress from the LASNEX-predicted free-surface velocity, to demonstrate reasonable agreement with the predicted stress histories. The inferred stress from the characteristics analysis of the LASNEX velocities is systematically slightly lower than the LASNEX stress. We consider this apparent underestimate as an additional systematic contribution to the stress uncertainty.

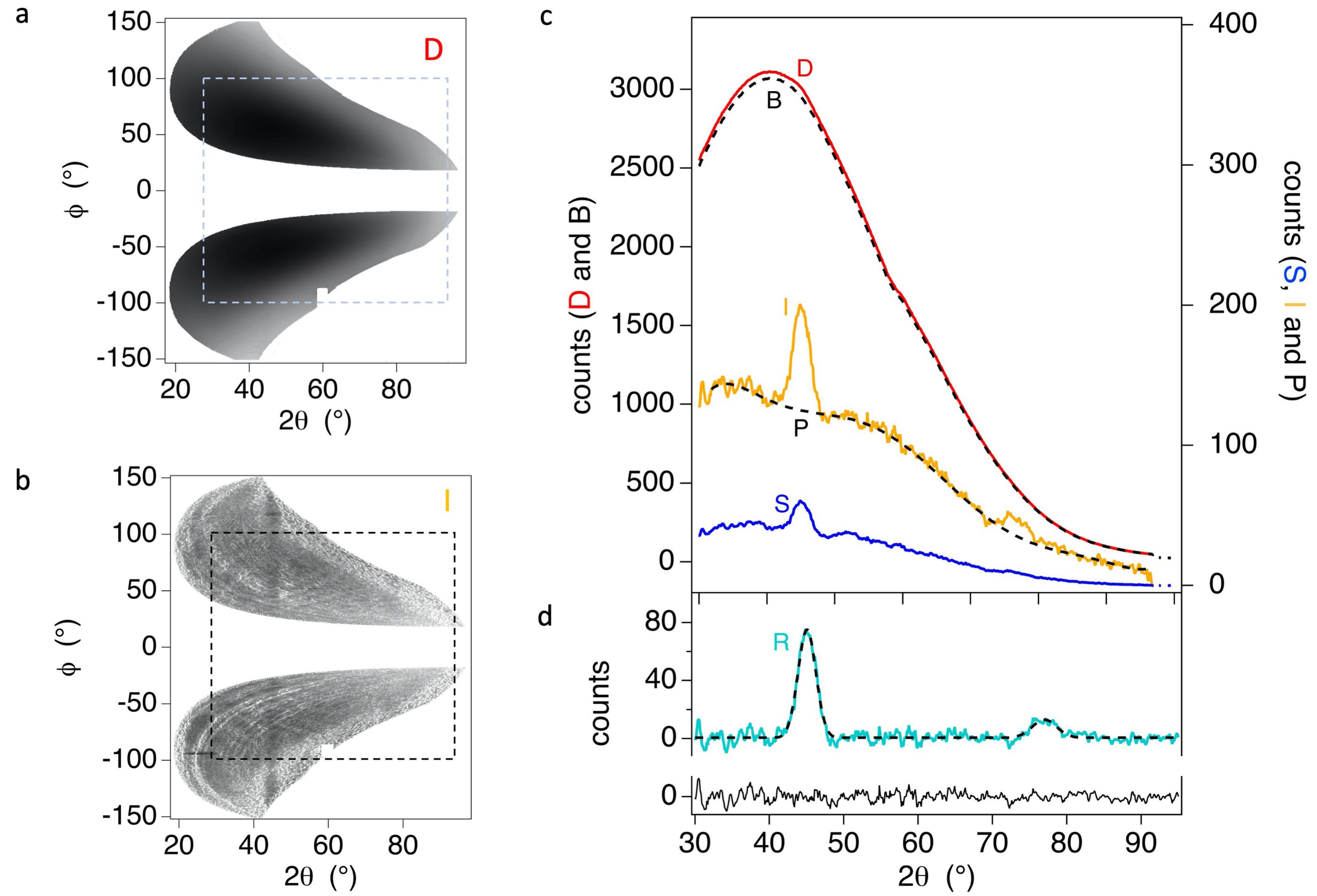

Extended Data Fig. 6 | Steps to subtract the X-ray background on the image plates. A lineout of the image plate from shot N170305 is shown, for illustration. **a**, Raw data, projected into ϕ (angle around the direct beam) versus 2θ (scattering angle) space. **b**, data after the SNIP background subtraction and intensity corrections (which take into account the variable transmission through the sample and image plate filter materials and the changing effective pinhole area depending on the angle of scattered X-rays) are applied. **c**, Image plate lineouts: the SNIP background (B) is subtracted from the raw data (D), yielding (S). Intensity corrections are then applied, yielding (I). At lower pressures (lower ablation-plasma background) this is often sufficient to flatten the background but when the laser power is very high, an additional polynomial background (P) is subtracted from (I) to generate the final result (R). **d** shows the diffraction pattern (R, teal line), a fit with Gaussian peak shapes and constant background (dashed black dashed line), and residual (solid black line). The centroids of the Gaussian peaks were used in a least-squares fitting to infer the FC8 density.

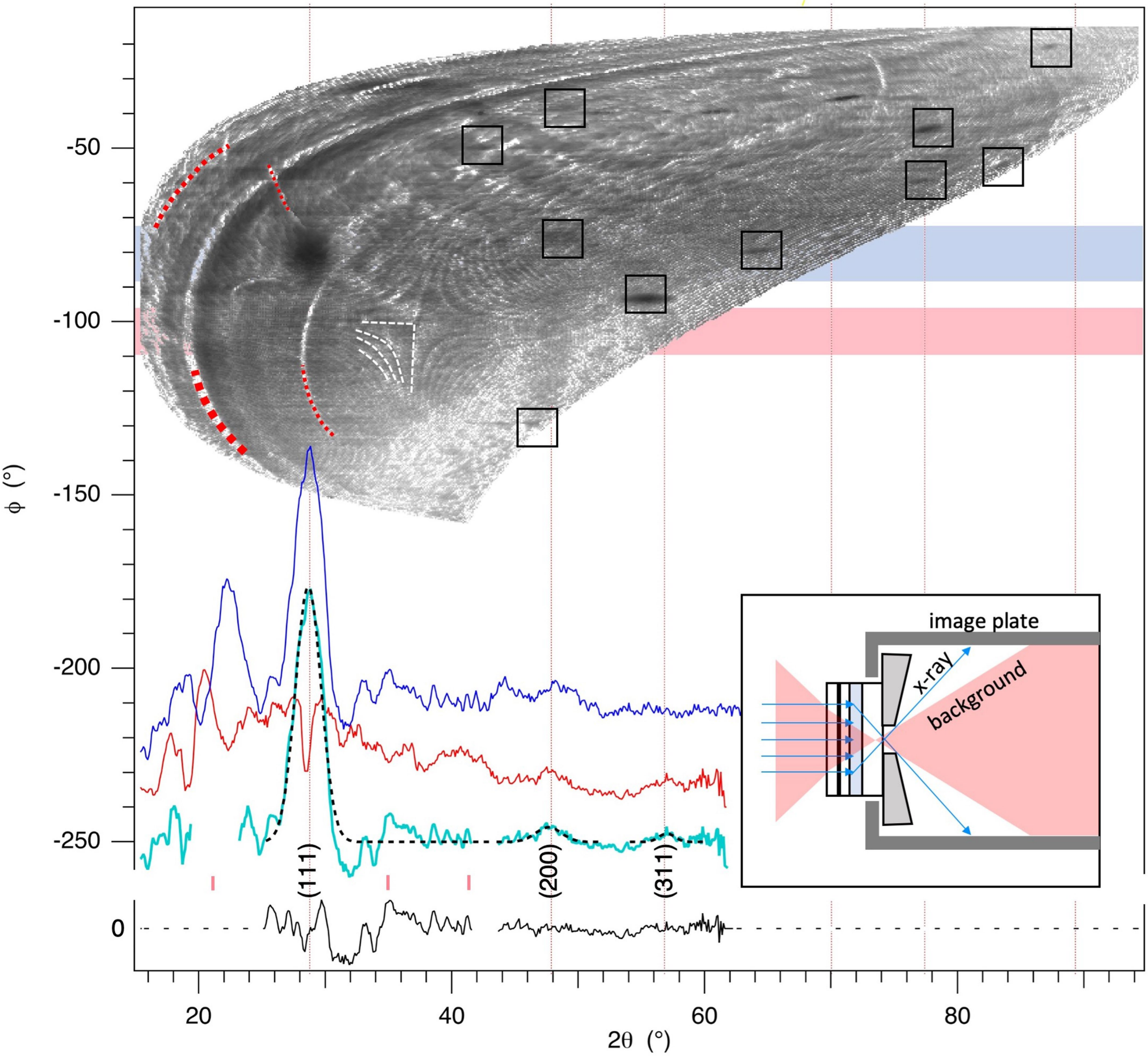

Extended Data Fig. 7 | Data extraction for shot N180214. At 2 TPa, the high drive background results in statistical noise levels that almost overwhelm the X-ray diffraction signal, so spurious features in the background show up clearly in the image plate lineouts. Some of the features are highlighted in this image: a pattern of Laue spots which originates from the broadband (modelled as 15–35 keV) Bremsstrahlung tail of the backlighter radiation, scattered off the uncompressed {110}-oriented single-crystal diamond window during the early X-ray source pulse (locations shown in black boxes); a series of bright bands, which are scanning artefacts, are marked with red dashed lines; and an aliasing pattern which arises from low sampling resolution is marked with white dashed lines (the sampling resolution is quite heterogeneous in this projection). As a result of all these spurious features, some diffraction lines that are evident by eye do not rise above the background noise in an average lineout over the entire image plate, and so we have chosen to stitch together narrower lineouts around the apparent diffraction lines. A narrow lineout over a region on the image plate highlighted in blue centred at about −80° is shown as the blue line. A single-crystal-like (111) diffraction line from diamond shows up above the background, because of its strong texture. Based on this texture, the line apparently originates from the single-crystal diamond tamper, which has reached pressure equilibrium with the sample over approximately half its volume by the time of the X-ray exposure. The (200) line and a fragment of the (311) line are largely too weak to register above the background noise from the ablation plasma, but they do show up in some regions of the image plate where the ablation plasma is shielded by the edge of the pinhole aperture, as illustrated by the cartoon inset. The X-rays from the ablation front that comprise the majority of the background are generated further from the pinhole than the Zr He$_\alpha$ X-rays scattered from the sample. There is consequently a narrow region on the image plate where the signal-to-noise ratio of the diffracted X-rays is higher, as shown in the narrow lineout centred near −100° (solid red line). The blue and red lineouts were stitched together, strong spurious features were masked out, and a polynomial background was subtracted, to create the teal-coloured diffraction pattern. The peaks evident by eye were fitted with Gaussian functions and the centroids used in a least-squares fit to infer the density. The residual is shown as the black solid line. The (311) peak position was not used in the least-squares fitting because it is so weak and so limited in azimuthal extent that its existence is questionable.

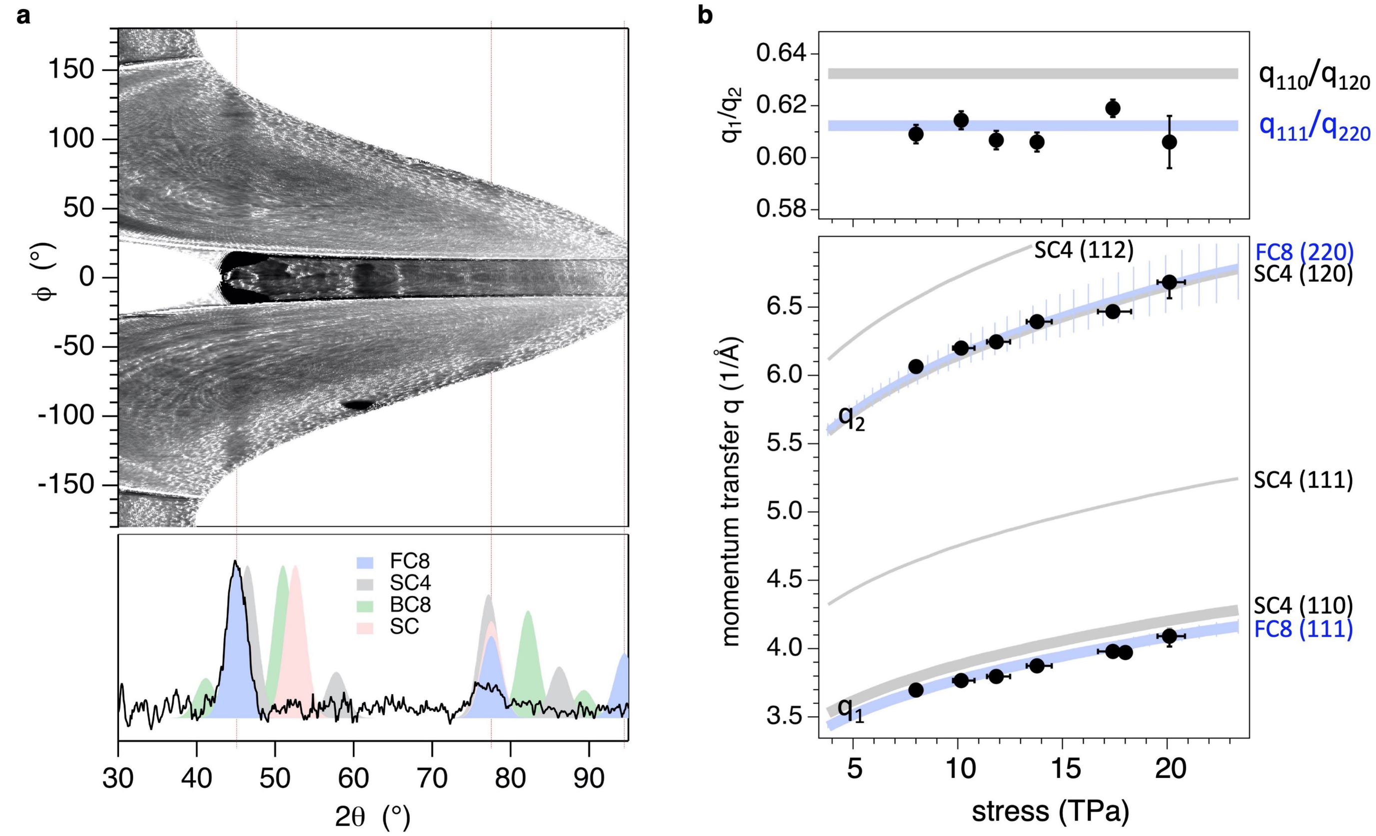

Extended Data Fig. 8 | Ruling out alternate phases. The observed diffraction peaks easily rule out a high-pressure BC8 or SC1 phase (ideal patterns shown in green and pink, respectively, in **a** for shot N170209), but the SC4 phase (grey) has peaks that come reasonably close to overlapping those of the FC8 (blue). All model diffraction patterns are plotted at 7.82 g cm^{-3} SC4 and FC8 peak positions are shown in **b**. The 'q_1' diffraction peak angle is several standard deviations away from the expectation for the SC4 phase (shown even more clearly in the plot of the ratio of peak positions q_1/q_2).

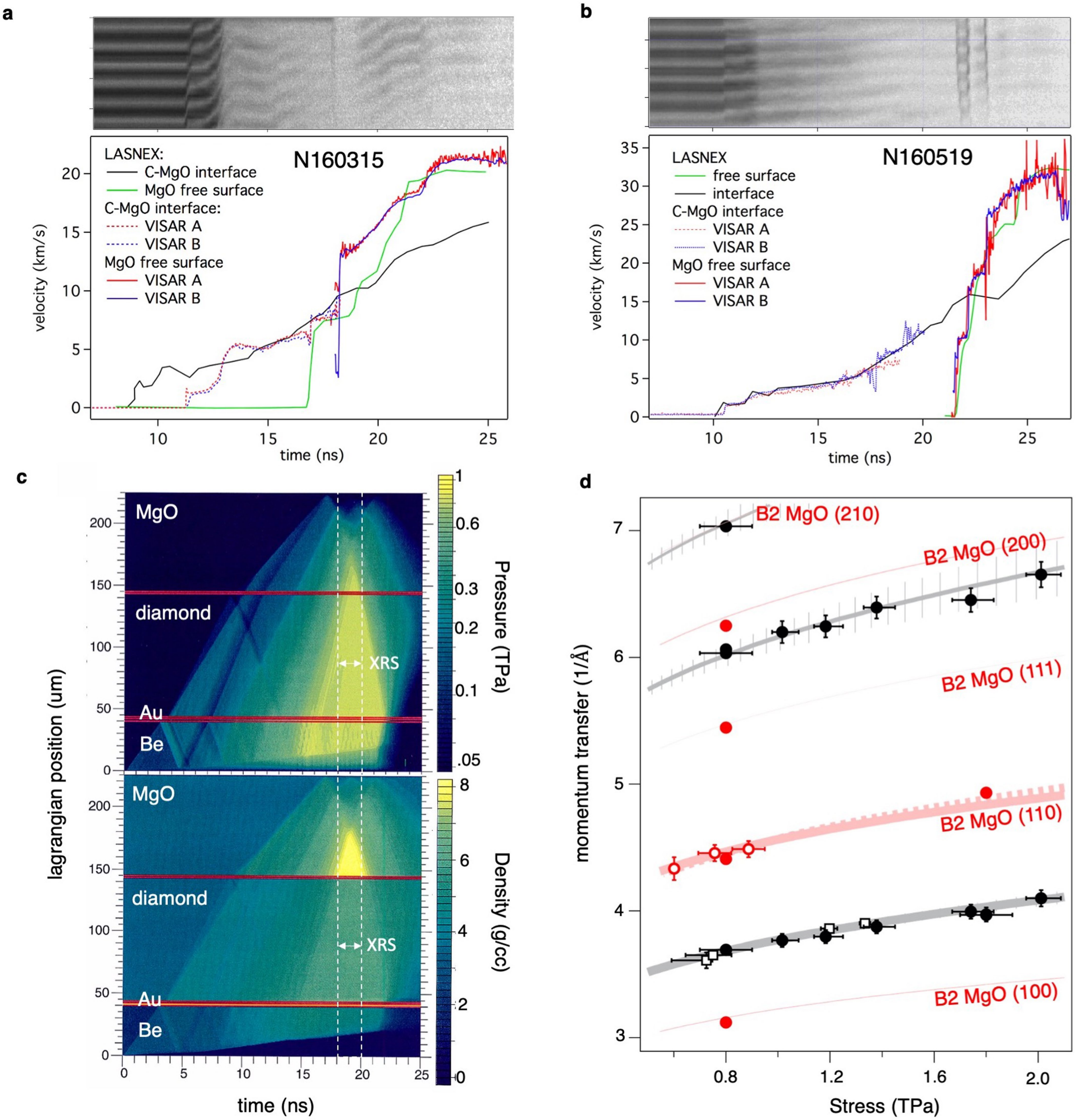

Extended Data Fig. 9 | MgO data summary. VISAR data from shots N160315 (**a**) and N160519 (**b**), which used MgO windows. The carbon–MgO interface can be tracked until the compression wave reaches the free surface, although the fringes lose substantial visibility, owing to the B1-to-B2 phase transformation in the MgO window. The ramp equation of state and index of refraction as a function of pressure are not yet well constrained for MgO, so the experimental stress is uncertain. The interface velocity shown here is corrected for the MgO index using an approximate Gladstone–Dale correction of 2.015 from the results of Vedam and Schmidt[51]. **c**, Radiation-hydrodynamic simulations of the stress and density histories across the sample for shot N160315. The X-ray source duration is bracketed by dashed white lines. These simulations show that, at the time of the experiment (that is, the duration of the X-ray source), 1/3 to 1/2 of the MgO window is in a uniform stress state at equilibrium with the diamond window, and the remaining volume is experiencing a strong stress gradient in which no single volume will diffract with sufficient intensity. We therefore report the peak positions in **d** at the same stress as the diamond sample. The pink contours in **d** show the ideal peak angles for B2 MgO as a function of pressure, taken from the equation of state reported by Coppari et al.[29] (data points shown as red triangles) and extrapolated to 2 TPa. The dashed contour, plotted for the B2 (110) peak only, shows the compressibility predicted for the principal adiabat by the Livermore tabulated equation of state model LEOS 219. We also show the peak positions reported to be from the diamond windows in a previous diffraction experiment[52] with open black symbols.

Extended Data Table 1 | Summary of experimental parameters and findings

	N160315	N150217	N150927	N150304	N170305	N161211	N180214
Target							
ablator	Be [48 μm]	Be [46 μm]	Be [47 μm]	Be [45 μm]	Be [47 μm]	Be [48 μm]	Be [56 μm]
heat shield	Au [2 μm]	Au [2 μm]	Au [2 μm]	Au [2 μm]	Au [6 μm]	Au [6 μm]	Zr [34 μm]
pusher		single crystal diamond [40 μm]	single crystal diamond [40 μm]	single crystal diamond [39 μm]			
sample	Micro-crystalline (>1 um grain size) CVD diamond [99 μm]	50-100 nm mono-crystalline diamond powder (52.4 vol%) + stycast 1266 epoxy [52 μm]	50-100 nm mono-crystalline diamond powder (53.2 vol%) + stycast 1266 epoxy [50 μm]	Micro-crystalline (>1 um grain size) CVD diamond [33 μm]	Micro-crystalline (>1 um grain size) CVD diamond [123 μm]	Micro-crystalline (>1 um grain size) CVD diamond [99 μm]	Micro-crystalline (>1 um grain size) CVD diamond [119 μm]
tamper	Single crystal MgO [80 μm]	single crystal diamond [149 μm]	single crystal diamond [148 μm]	single crystal diamond [148 μm]	single crystal diamond [189 μm]	Single crystal MgO [125 μm]	single crystal diamond [198 μm]
Stress (TPa)	0.8*	1.02 (-0.04/+0.06)	1.18 (-0.04/+0.07)	1.38 (-0.05/+0.07)	1.74 (-0.07/+0.09)	1.8*	2.01 (-0.06/+0.07)
Histogram width (TPa)		0.09	0.16	0.12	0.006		0.06
Structural parameters							
FC8:							
density (g/cm^3)	6.31(0.12)	6.74(0.04)	6.89(0.13)	7.34(0.15)	7.80(0.06)	7.76(0.05)	8.39 (+0.05/-0.43)
q_{111} (A^{-1})	3.694(0.018)	3.802(0.018)	3.790(0.019)	3.869(0.020)	3.995(0.018)	3.972(0.017)	4.09 (-0.08/+0.03)
q_{220} (A^{-1})	6.064(0.026)	6.187(0.026)	6.245(0.027)	6.383(0.027)	6.454(0.025)		6.68 (-0.12/+0.04)
q_{113} (A^{-1})	7.034(0.03)						
MgO:							
density (g/cm^3)	8.30(0.08)					11.45(0.05)	
q_{100} (A^{-1})	3.121(0.018)						
q_{110} (A^{-1})	4.415(0.017)					4.933(0.016)	
q_{111} (A^{-1})	5.440(0.032)						
q_{200} (A^{-1})	6.271(0.035)						

Target dimensions are shown, with part thicknesses indicated in square brackets. The Au heat shield was coated directly onto the beryllium (Be) ablator, and the rest of the parts were held together by micrometre-scale layers of Stycast 1266 epoxy, for all targets except N150927 and N150304. For these two targets the diamond–Stycast slurry was pressed and cured between the diamond pusher and tamper, requiring no additional glue bond. All the single-crystal diamonds were {110}-oriented and the microcrystalline chemical-vapour-deposition diamond has a {110} fibre texture. The stress in the sample is reported (for the two cases marked with asterisks, the stress is inferred for radiation hydrodynamic simulations), and the FWHM of a histogram of stress states across the entire sample thickness, over the duration of the 2-ns X-ray measurement. Densities and X-ray peak angles (in units of momentum transfer) are reported for diamond, and for the MgO, in the case where MgO was used as a tamper material.